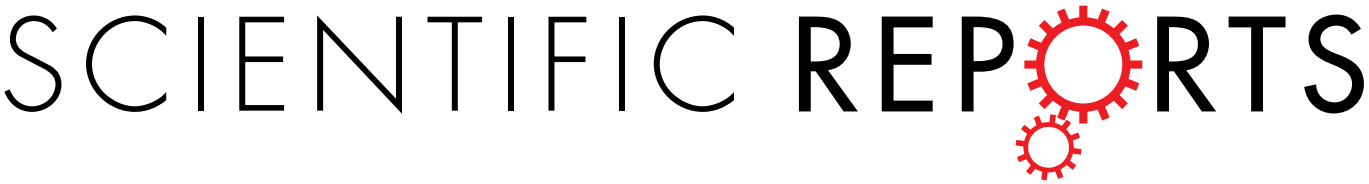

OPEN

The Effect of Crystal Face of Fe_2O_3 on the Electrochemical Performance for Lithium-ion Batteries

Received: 11 April 2016
Accepted: 17 June 2016
Published: 06 July 2016

Minmin Chen[1,*], Enyue Zhao[1,*], Qingbo Yan[1], Zhongbo Hu[1], Xiaoling Xiao[1] & Dongfeng Chen[2]

Fe_2O_3 nanorods exposing (001) and (010) plane as well as Fe_2O_3 nanosheets exposing (001) plane have been successfully synthesized. Fe_2O_3 nanosheets exhibit better cycle performance and rate capabilities than that of Fe_2O_3 nanorods. The discharge capacity of Fe_2O_3 nanosheets can stabilize at 865 mAh/g at the rate of 0.2 C (1C = 1000 mA/g) and 570 mAh/g at the rate of 1.2 C after 80 cycles, which increased by 90% and 79% compared with 456 mAh/g and 318 mAh/g of Fe_2O_3 nanorods. In comparison with (010) plane, the (001) plane of hematite possesses larger packing density of Fe^{3+} and O^{2-}, which is responsible for the superior electrochemical performances of Fe_2O_3 nanosheets than that of Fe_2O_3 nanorods. In addition, potentiostatic intermittent titration (PITT) results show the diffusion coefficients of Li^+ (D_{Li}) of Fe_2O_3 nanosheets is higher than that of Fe_2O_3 nanorods. The higher diffusion coefficients of Li^+ is favorable for the excellent lithium-storage capabilities and rate capability of Fe_2O_3 nanosheets. Inspired by our results, we can design and synthesize Fe_2O_3 or other electrodes with high performances according to their structure features in future.

3d transition-metal oxides, which can be used as anode materials, such as iron oxide, cobalt oxide, and nickel oxide have attracted a great deal of attentions for their much higher capacity than that of conventional graphite (372 $mAhg^{-1}$)[1–12]. For instance, the theoretical capacity of Co_3O_4 is about 890 $mAhg^{-1}$, which is almost two and a half times higher than that of graphite. However, high price and toxicity of Co limit the application of Co_3O_4[13,14]. Interestingly, Fe_2O_3 also exhibits high capacity (1007 $mAhg^{-1}$) like Co_3O_4. More importantly, due to its low cost, nontoxicity and high resistance to corrosion, Fe_2O_3 has attracted special attentions in recent years[15,16]. For example, various morphologies of Fe_2O_3 such as nanoparticles, nanotubes, hollow structure and thin films have been studied as electrodes for lithium-ion batteries[17–25]. Lou *et al.* prepared a series of hollow microspheres of iron oxides which showed significantly improved lithium-storage capabilities[24,25]. In addition to the above-mentioned methods, many studies have proved that the crystal plane structure of electrode materials has a significant effect on the electrochemical properties. Islam *et al.* reported that the (010) plane of $LiFePO_4$ is a favorable plane for fast Li^+ transport[26]. Wei *et al.* found that the electrochemical performance of lithium rich material $Li(Li_{0.17}Ni_{0.25}Mn_{0.58})O_2$ with (010) and (100) planes have been greatly increased, exhibiting not only a high reversible capacity but also an excellent cycle stability[27]. Huang *et al.* found the facet-dependent electrochemical properties of Co_3O_4 toward heavy metal ions and found that the Co_3O_4 nanoplates with (111) facet performed better electrochemical sensing capability than the Co_3O_4 nanocubes with (001) facet[28]. Not long ago, we also reported the facet-dependent electrochemical capability of Co_3O_4 as anode material for Li-ion batteries and proved the Co_3O_4 octahedron with exposed (111) plane exhibited more excellent electrochemical properties than that of Co_3O_4 cube with exposed (001) plane and Co_3O_4 truncated octahedron with exposed (001) and (111) planes[29]. Therefore, studies on the crystal plane controllable synthesis of nanomaterials are of great interest and are actively being pursued. So, controlling the exposed crystal plane of Fe_2O_3 might also be an effective strategy to further improve the electrochemical performance of Fe_2O_3 as anode materials for lithium-ion batteries.

[1]College of Materials Science and Opto-electronic Technology University of Chinese Academy of Sciences, Beijing 100049, P. R. China. [2]China Institute of Atomic Energy, Beijing 102413, P. R. China. *These authors contributed equally to this work. Correspondence and requests for materials should be addressed to X.X. (email: xlxiao@ucas.ac.cn) or D.C. (email: dongfeng@ciae.ac.cn)

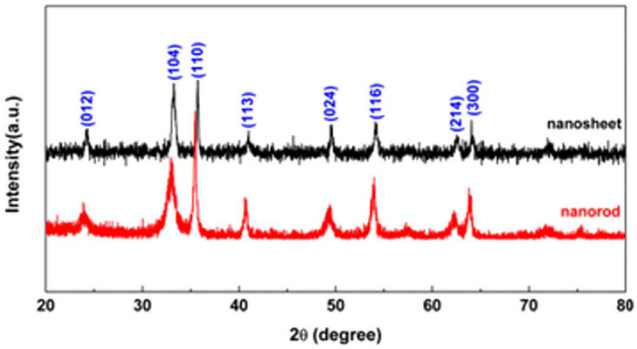

Figure 1. Powder X-ray diffraction patterns of Fe_2O_3 nanorods and nanosheets in a 2θ range of 10–80°.

In this article, we successfully synthesized two kinds of Fe_2O_3 with exposed different crystal plane, including nanorods with (001) and (010) plane and nanosheets with the (001) plane. Interestingly, when used as anode materials in lithium-ion batteries, Fe_2O_3 nanosheets exhibit better cycle performance and rate capabilities than that of Fe_2O_3 nanorods. To be specific, the discharge capacity of Fe_2O_3 nanosheets could stabilize at 865 $mAhg^{-1}$ at the rate of 0.2C (1 C = 1000 mAg^{-1}) and 570 $mAhg^{-1}$ at the rate of 1.2 C over 80 cycles, which increased by 90% and 79% compared with 456 $mAhg^{-1}$ and 318 $mAhg^{-1}$ of Fe_2O_3 nanorodes. Herein, the outstanding electrochemical performance of Fe_2O_3 nanosheets can be attributed to the highly exposed (001) planes. Crystal structure have revealed that the (001) plane possesses larger packing density than that of (010) plane, and the crystal effect is the crucial reason for the differences of electrochemical performance[30]. On the other hand, potentiostatic intermittent titration (PITT) results show that Fe_2O_3 nanosheets have higher diffusion coefficient of Li^+ (D_{Li}) and are more favorable for the diffusion of lithium ion.

To the best of our knowledge, we, for the first time, combined electrochemical experiment and crystal structure analysis to elucidate exposed crystal plane-electrochemical properties relationship of Fe_2O_3 as anode for rechargeable lithium ion batteries. Our results indicate the superior electrochemical performances of Fe_2O_3 nanosheets can be attributed to (1) the larger packing density of Fe^{3+} and O^{2-} of (010) plane and (2) the higher diffusion coefficient of Li^+ (D_{Li}) of Fe_2O_3 nanosheets during discharge-charge process. Furthermore, our results provide a idea which we can design and synthesize electrode materials with high performances according to their structure features in future.

Results

In Fig. 1, the indexed X-Ray Diffraction (XRD) patterns of Fe_2O_3 samples show that the diffraction peaks match well with the standard PDF card (JCPDS no. 86–2368), indicating the purity of the products and the two kinds of Fe_2O_3 belong to the same space group. The exposed facets of nanosheets and nanorodes have been determined by high resolution transmission electron microscopy (HRTEM) characterization in Fig. 2c–h. The clear lattice spacing and fast Fourier transform selected-area electron diffraction (FFT-SAED) patterns indicate that Fe_2O_3 nanosheets and nanorods are single crystalline. Figure 2c shows the TEM image of a Fe_2O_3 nanosheet, and the corresponding SAED pattern is shown in Fig. 2d. It can be clearly seen that the exposed crystal facet is perpendicular to the (3000), (0300) and (0030) facets of Fe_2O_3 nanosheets, and the interlayer spacings of 0.252 nm inserted in Fig. 1c correspond to the (110) plane of the Fe_2O_3. Thus it can be concluded that the exposed facets of the nanosheets are (001). Figure 2e and f show the similar interlayer spacings and SAED pattern compared with the Fe_2O_3 nanosheets, which indicate that one of the exposed facets of the Fe_2O_3 nanorods are (001). Figure 2g shows the TEM image of another facet of Fe_2O_3 nanorodes and the corresponding SAED pattern is shown in Fig. 2h. The SAED pattern in Fig. 2h shows that the exposed crystal facet is perpendicular to the (300), (006) and (202) facets of the Fe_2O_3, and the interlayer spacings of 0.210 nm inserted in Fig. 2g correspond to the (202) plane of the Fe_2O_3.

So another exposed facets of the nanorodes are (010). The structural models of Fe_2O_3 nanorod is displayed in Fig. 3c, the exposed (001) and (010) crystal facets can be clearly shown and the models of Fe_2O_3 nanosheet is showed in Fig. 3f. Figure 3a,d show the SEM images of Fe_2O_3 nanorodes and nanosheets, respectively. It can be seen that the average length of Fe_2O_3 nanorods is about 500 nm, the width and thickness is about 50 and 15 nm, respectively. The average diameter and thickness of Fe_2O_3 nanosheets is about 200 nm and 15 nm, respectively. The Fe_2O_3 nanosheets and nanorods of nanosize can reduce the diffusion length of Li^+ ions and increase reactivity of the material, which are very favorable for excellent electrochemical performances.

Subsequently, the comparison galvanostatic discharge capacities of Fe_2O_3 nanorods and nanosheets in a potential range of 0.1–3.0 V (vs Li/Li^+) at a rate of 0.2 C were comprehensively investigated and illustrated in Fig. 4a–c. It can be seen from Fig. 4a that Fe_2O_3 nanorod and Fe_2O_3 nanosheet electrodes deliverer approximately a discharge capacity of 1135 $mAhg^{-1}$ and 1210 $mAhg^{-1}$ in the first cycle, respectively. After that the discharge capacity decreases rapidly, and the reason can be ascribed to the change of structure during the initial charge-discharge process. From the beginning of the second cycle, two kinds of Fe_2O_3 electrodes exhibit good cycle stability until to the 20 cycles. Surprisingly, after 20 cycles, the discharge capacity of the Fe_2O_3 nanorods monotonically decline, while the discharge capacity of Fe_2O_3 nanosheets slightly increase. Similar phenomenon also has been found in the case of CoO and Co_3O_4 as well as other Fe_2O_3 reports in the literature, though a clear understanding has not

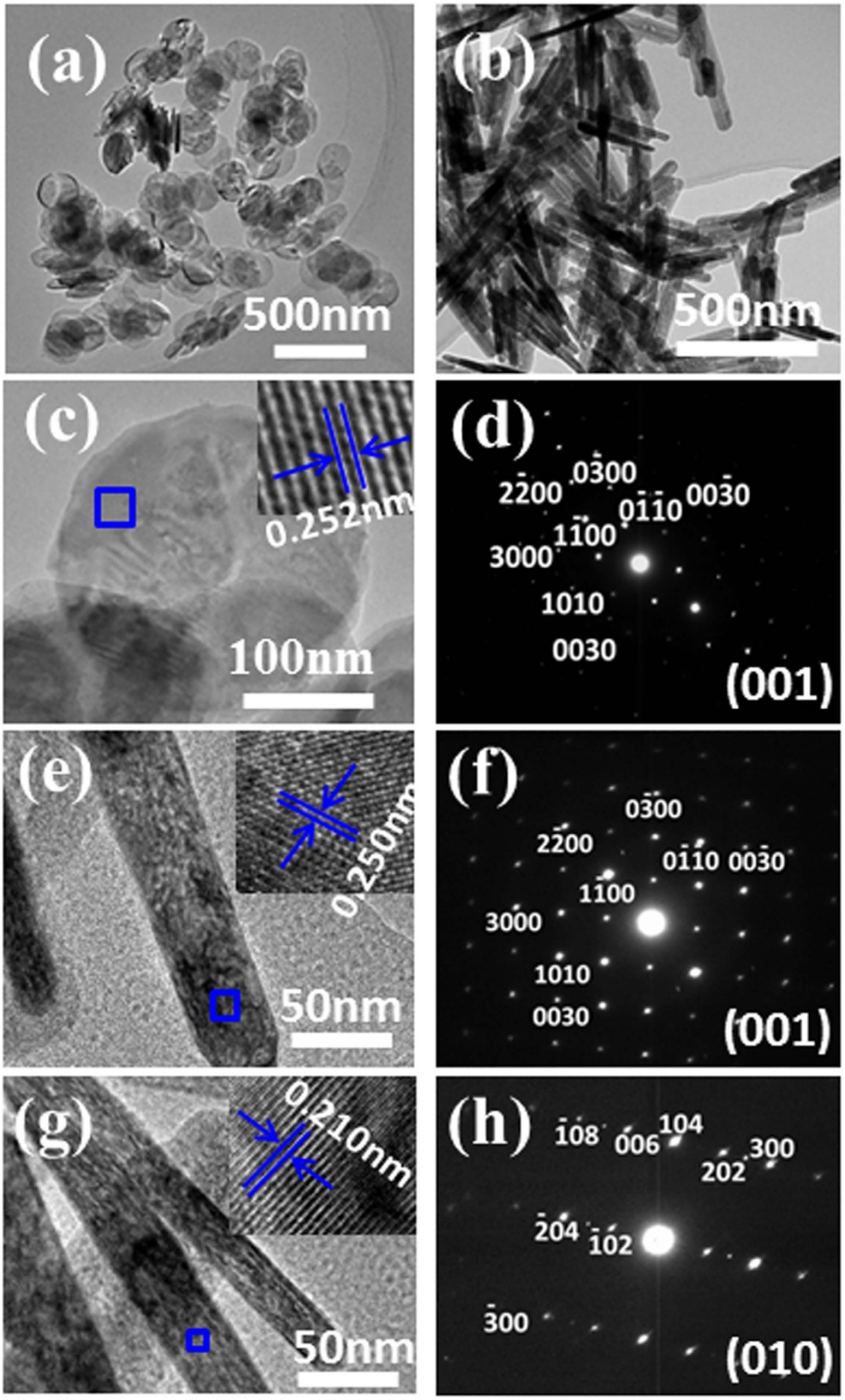

Figure 2. TEM images of Fe_2O_3 nanosheets (**a**) and Fe_2O_3 nanorods (**b**); (**c,d**) The TEM image of a Fe_2O_3 nanosheet, inset shows the lattice fringes and the corresponding SAED pattern; (**e,f**) The TEM image of Fe_2O_3 nanorode with {001} plane, inset shows the lattice fringes and the corresponding SAED pattern; (**g,h**) The TEM image of Fe_2O_3 nanorode with {010} plane, inset shows the lattice fringes and the corresponding SAED pattern.

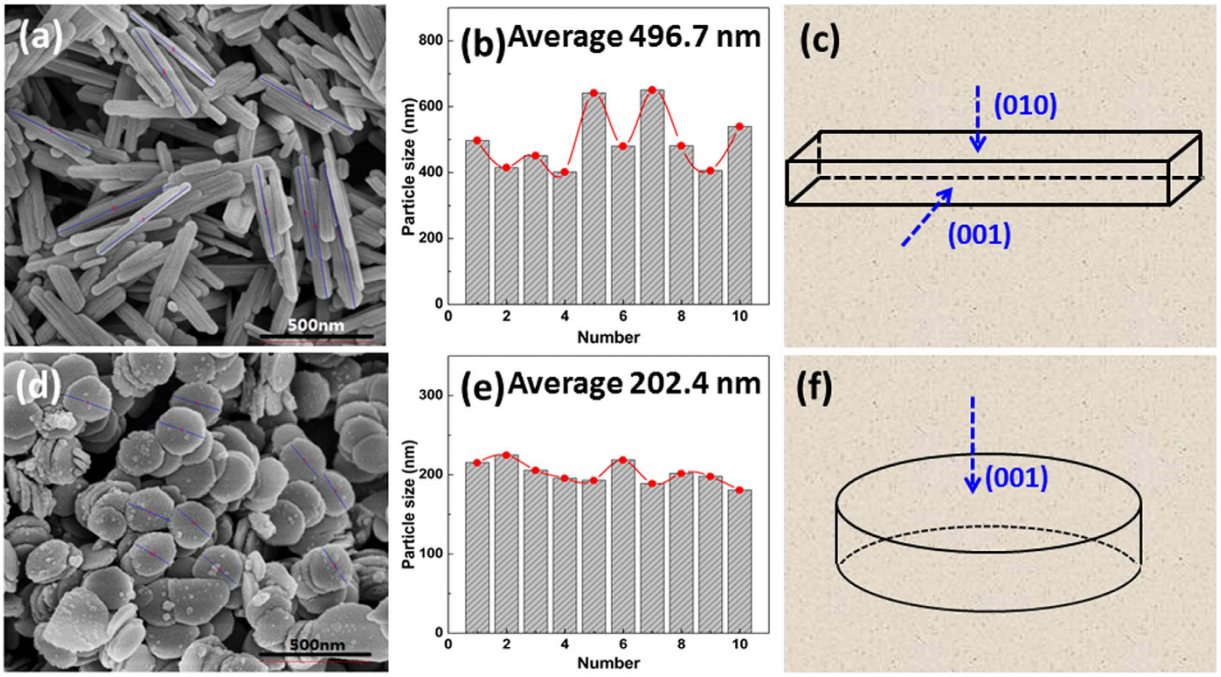

Figure 3. The SEM images and crystal size distribution histogram of (**a,b**) Fe_2O_3 nanorods and (**d,e**) Fe_2O_3 nanosheets; Structural models of (**c**) Fe_2O_3 nanorods and (**f**) Fe_2O_3 nanosheets.

been obtained[31–33]. As shown in Fig. 4a, the discharge capacity of the Fe_2O_3 nanosheets maintains at 865 $mAhg^{-1}$ with a capacity retention of 95.3% after 80 cycles, in contrast, the discharge capacity of Fe_2O_3 nanorods maintains at 456 mAh/g with a capacity retention of 50.7% after 80 cycles.

Figure 4d shows the rate performance of Fe_2O_3 nanorods and nanosheets. Specifically, the discharge capacity of Fe_2O_3 nanorods at 0.2, 0.4, 0.8, 1.2, 1.6, 2.0 and 2.4 C are 896, 763, 627, 544, 478, 430 and 385 $mAhg^{-1}$, respectively. The corresponding values for the Fe_2O_3 nanosheets were 966, 832, 734, 667, 628, 586 and 550 $mAhg^{-1}$, respectively. By comparing the discharge capacity of the two samples, Fe_2O_3 nanosheets display higher capacity than Fe_2O_3 nanorods at various charge−discharge rates from 0.2 to 2.4 C. Meanwhile, as the growth of charge–discharge current density, the gap between the discharge capacities of the Fe_2O_3 nanorods and nanosheets samples became larger. For instance, the discharge capacity of Fe_2O_3 nanosheets increase by 8% compared with that of Fe_2O_3 nanorods at 0.2 C, while the discharge capacity increase by 43% at the rate of 2.4 C. In addition, it should be noted when the rate was returned back to the 0.2 C, Fe_2O_3 nanosheets still show higher discharge capacity than that of Fe_2O_3 nanorods. At the recovery rate of 0.2 C, both Fe_2O_3 nanosheets and nanorods display lower discharge capacity compared with the initial capacity at 0.2 C. The phenomenon is due to the destruction of crystal structure of Fe_2O_3 during discharge-charge cycle process.

In order to research the cycle stability under high current density, the Fe_2O_3 nanorods and nanosheets are tested at the rate of 1.2 C, as shown in Fig. 4e–g. Obviously, the electrode of Fe_2O_3 nanosheets shows much higher discharge capacity than that of Fe_2O_3 nanorods at high rate. Especially, the discharge capacity of Fe_2O_3 nanosheets can reach 719 $mAhg^{-1}$ after 150 cycles. This value is 71% higher than that of Fe_2O_3 nanorods, which only shows 419 $mAhg^{-1}$ after 150 cycles.

SEM and TEM images of Fe_2O_3 nanosheets and nanorods samples after extensive cycling are shown in Fig. 5. It can be clearly seen in Fig. 5a,c that Fe_2O_3 nanosheets keep relatively complete sheet structure after extensive charge-discharge cycling. Similar to nanosheets, Fe_2O_3 nanorods also show well virgulate shape which can be seen in Fig. 5b,d. In addition, there is no significant change of the Fe_2O_3 particle size after charge-discharge cycling.

It is reported that the Brunauer–Emmett–Teller (BET) surface areas of electrode materials play a improtant role on the electrochemical performance of lithium ions batteries[34]. Our nitrogen-sorption analysis reveals that the BET specific surface areas of Fe_2O_3 nanorods and Fe_2O_3 nanosheets were 26.81 and 18.25 m^2/g, respectively (Fig. 6). The BET specific surface areas of Fe_2O_3 nanorods is larger than that of Fe_2O_3 nanosheets, whereas, the Fe_2O_3 nanosheets exhibit better electrochemical properties compared with Fe_2O_3 nanorods. So it can be concluded that the effect of specific surface areas of electrodes on the difference of electrochemical properties between Fe_2O_3 nanosheets and nanorodes can be overlooked.

Evidently, the electrochemical performances of lithium ion batteries are related to the intrinsic crystal structure[35]. So the crystal structure of Fe_2O_3 is analyzed. For Fe_2O_3 samples, the (001) plane has been found possessing the larger packing density, in which Fe^{3+} and O^{2-} ions pack layer by layer. Specifically, the packing densities of the Fe^{3+} and O^{2-} are 9.11 nm^{-2} and 13.8 nm^{-2}, respectively. In contrast, the packing densities of the (010) facets for ions are 2.89 nm^{-2} and 5.78 nm^{-2}. Due to the high atomic density, more Fe^{3+} ions participate in the reaction, and lead to a high specific capacity[28]. The detailed crystal structure of Fe_2O_3 have been displayed in Fig. 7. Meanwhile, it can be seen from the model of Fe_2O_3 nanosheets and nanorodes in Fig. 7, that the proportion of (001) plane in

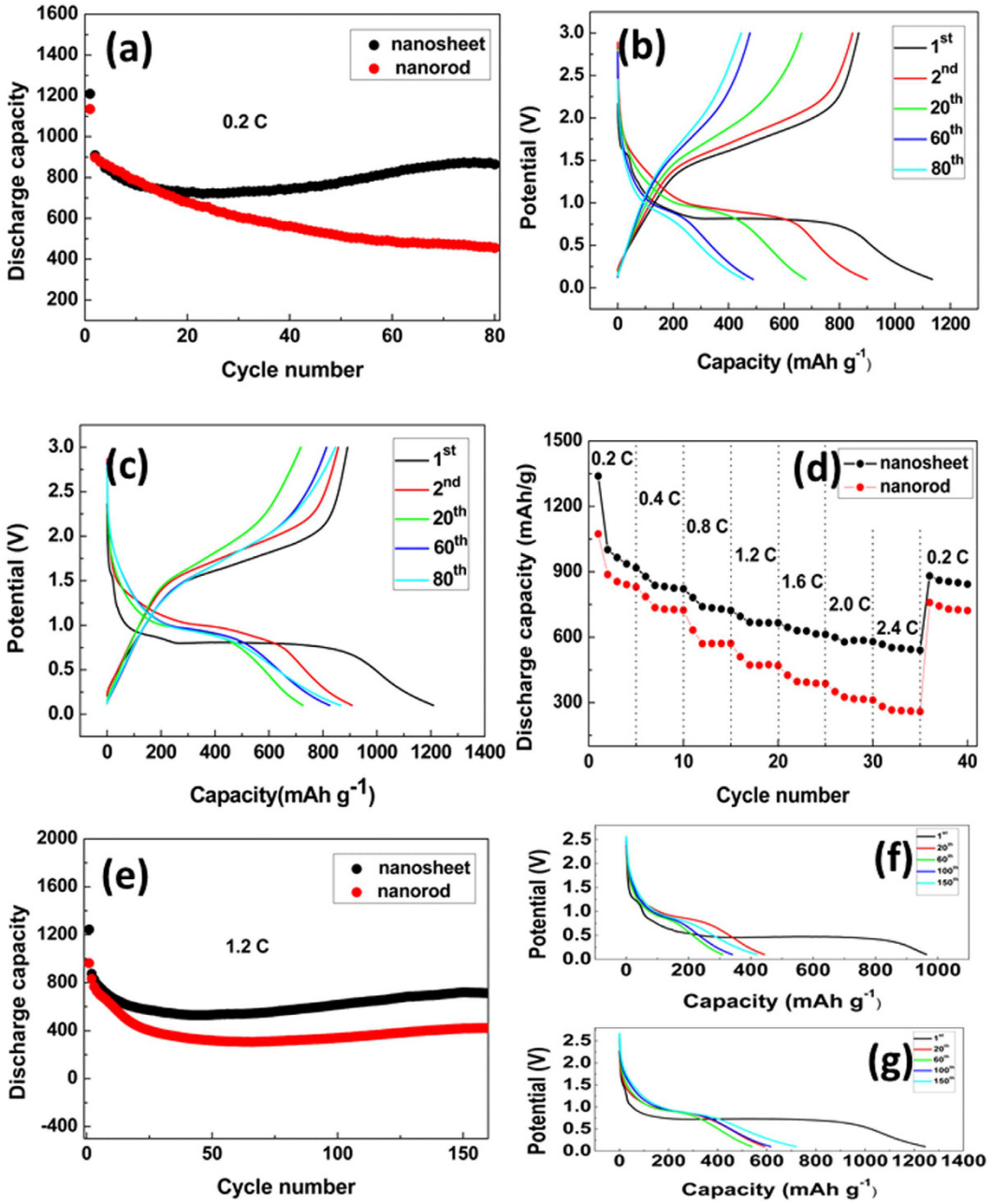

Figure 4. N_2 absorption curves of Fe_2O_3 nanosheets and Fe_2O_3 nanorods. (**a**) Comparison of cycling performance of the two kinds of Fe_2O_3 at the rate of 0.2 C; The charge/discharge curves of (**b**) Fe_2O_3 nanorods and (**c**) Fe_2O_3 nanosheets in the 1st, 2nd, 20th, 60th and 80th cycles at the rate of 0.2 C, respectively. (**d**) The rate performances of Fe_2O_3 nanorods and Fe_2O_3 nanosheets. (**e**) Plots of the specific discharge capacity vs. cycle number for the Fe_2O_3 nanostructure electrode at the rate of 1.2 C; The discharge curves of (**f**) Fe_2O_3 nanorods and (**g**) Fe_2O_3 nanosheets in the 1st, 20th, 60th, 100th and 150th cycles at the rate of 1.2 C, respectively.

nanosheet is almost 100%, while in nanorodes is about 23%. And the mainly exposed crystal plane is (010) facet in nanorodes, in which the proportion of (010) plane is about 77%. The results indicate that the Fe_2O_3 samples which exposed more (001) plane show a superior electrochemical capability.

Figure 8 shows Nyquist plots of the two kinds of Fe_2O_3 electrode measured at the open circuit potential and an equivalent circuit proposed to fit the spectra. As can be seen from Table 1, the charge transfer resistances (R_{ct}) for Fe_2O_3 nanosheets (53 Ω) is much smaller than that obtained from the Fe_2O_3 nanorodes (179 Ω) electrode. The electrochemical impedance spectroscopy (EIS) data indicates that Fe_2O_3 nanosheets possesses smaller lithium ion migration resistance and is more conducive to the rapid migration of lithium ions.

For the sake of confirming D_{Li} in electrode materials, PITT measurement was performed. Figure 9a–c display the PITT results of Fe_2O_3 samples before discharge-charge cycle. It can be seen the D_{Li} of Fe_2O_3 nanosheets is about one time higher than that of Fe_2O_3 nanorods. Figure 9d–f display the PITT results of Fe_2O_3 samples after a

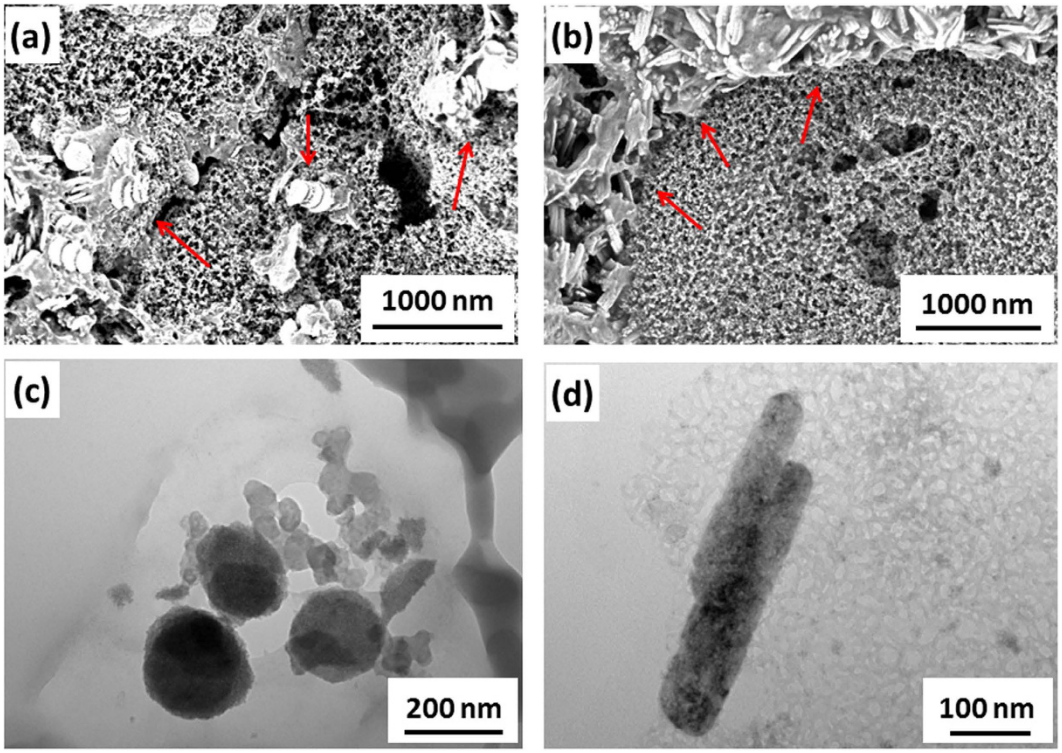

Figure 5. SEM and TEM images of (**a,c**) Fe_2O_3 nanosheets and (**b,d**) Fe_2O_3 nanorods after 30 cycles at 0.2 C.

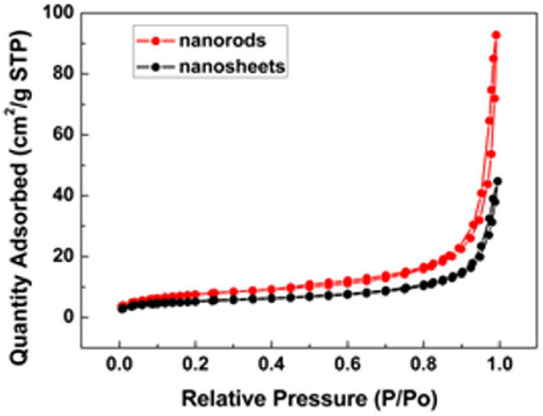

Figure 6. N2 absorption curves of Fe_2O_3 nanosheets and Fe_2O_3 nanorods.

circle of discharge-charge cycle at the current density of 200 mA/g. It is obviously that D_{Li} of Fe_2O_3 nanosheets are higher than that of Fe_2O_3 nanorods. For instance, the D_{Li} average value of Fe_2O_3 nanosheets is 2.2×10^{-10} cm^2 s^{-1} which increased by 15.7%, compared to 1.9×10^{-10} cm^2 s^{-1} of Fe_2O_3 nanorods. The improved kinetic parameters D_{Li}, indicate that Fe_2O_3 nanosheets possess higher lithium diffusion coefficient. For this reason, Fe_2O_3 nanosheets show better rate capability, as shown in Fig. 4d. Figure 4d show that Fe_2O_3 nanosheets with (001) planes possess higher discharge capacity not only at the low rate of 0.2 C but also at the high rate of 1.2 C. Additional, the Fe_2O_3 nanosheets with (001) planes exhibit better cycle stability and rate ability. Generally, the Fe_2O_3 nanosheets with (001) plane exhibit better electrochemical properties than that of the Fe_2O_3 nanorods with (010) and (001) planes.

In conclusion, we successfully synthesized two kinds of morphology of single crystal Fe_2O_3 with exposed different crystal plane, including nanorods with (001) and (010) plane and nanosheets with the (001) plane. Fe_2O_3 nanosheets exhibit better cycle performance and rate capabilities than that of Fe_2O_3 nanorods. The reasons can be attributed to that (1) the larger packing density of Fe^{3+} and O^{2-} of (010) plane and (2) the higher diffusion coefficient of Li^+ (D_{Li}) of Fe_2O_3 nanosheets during discharge-charge process. Our studies indicate that the crystal structure has a very important influence on the electrochemical performances, which may be helpful for developing high performance lithium ion batteries.

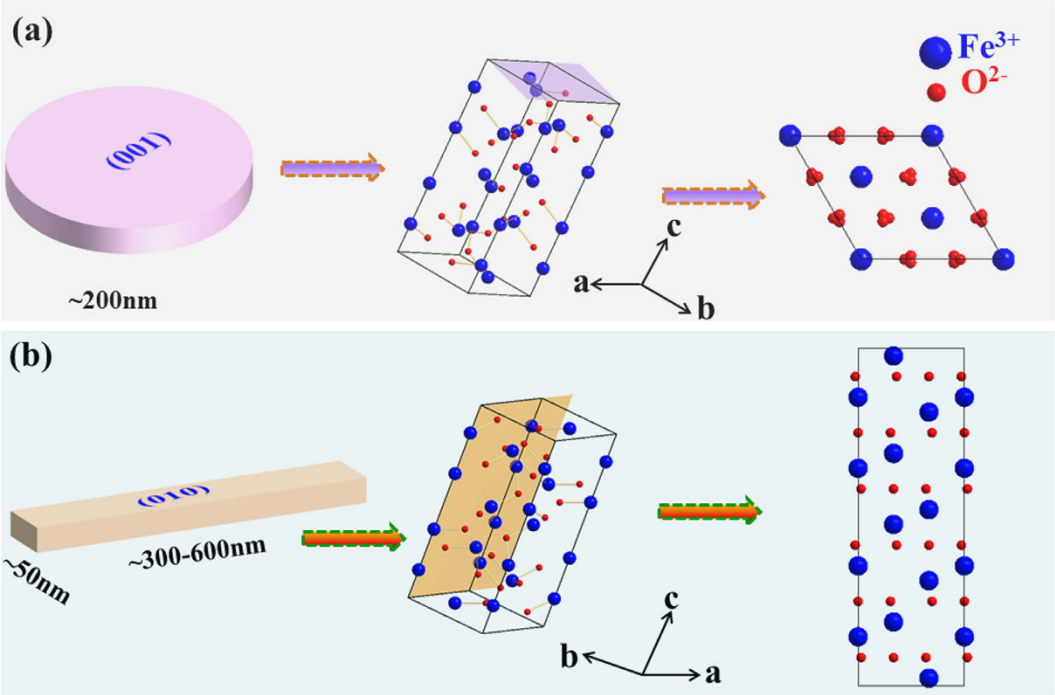

Figure 7. The surface atomic configurations in (**a**) the (001) plane and schematic hematite structure projected along {001}, (**b**) the (010) plane and schematic hematite structure projected along {010}. The Fe_2O_3 Crystallographic Information File (CIF) was taken from the NIST/FIZ FindIt Inorganic Crystal Structure Database.

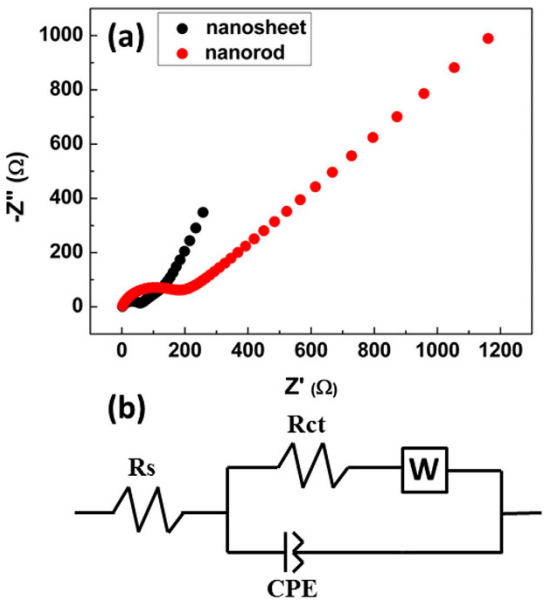

Figure 8. (**a**) Nyquist plots for Fe_2O_3 nanorods and Fe_2O_3 nanosheets; (**b**) The corresponding equivalent circuit.

Sample	R_S		R_{ct}	
	Value (Ω)	Error %	Value (Ω)	Error %
Fe_2O_3 nanorods	1.2388	26.4	178.7	4.346
Fe_2O_3 nanosheets	1.7051	6.436	53.337	2.482

Table 1. The fitted solution resistances (R_s) and charge transfer resistances (R_{ct}) for the Nyquist plots of Fe_2O_3 nanorods and nanosheets.

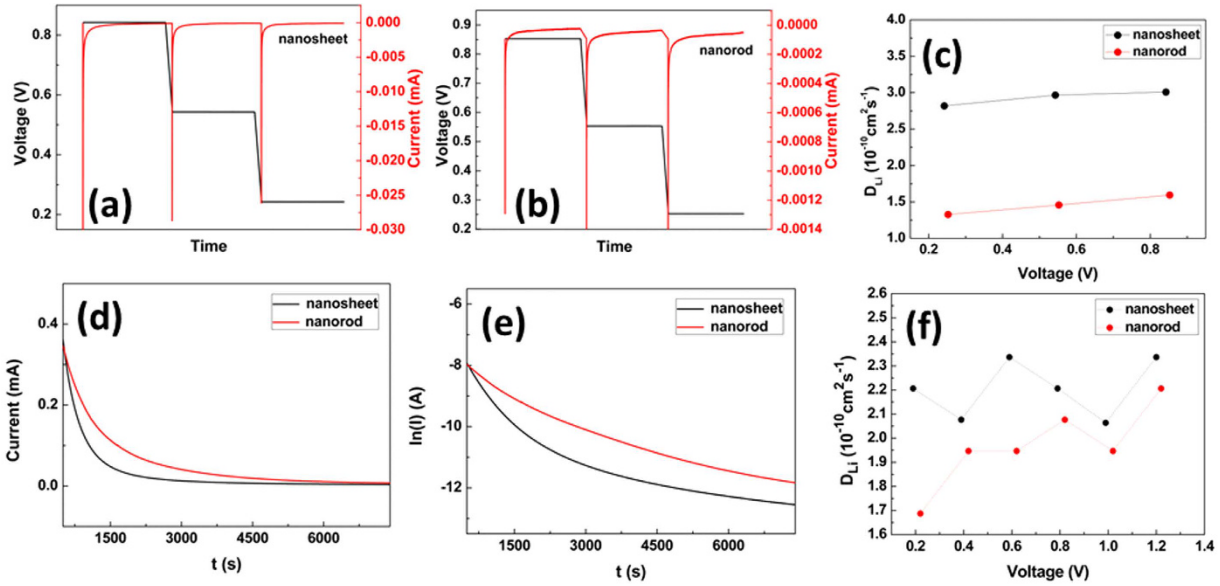

Figure 9. PITT curves of (**a**) Fe_2O_3 nanosheets and (**b**) Fe_2O_3 nanorods and (**c**) diffusion coefficients of Li^+ (D_{Li}) before discharge-charge cycle; Current-time transient plots of PITT for a potential step of 1.0–0.8 V after one cycle, (**d**) I vs. t and (**e**) ln(I) vs. t; (**f**) D_{Li} of Fe_2O_3 nanorods and Fe_2O_3 nanosheets during discharge processe.

Methods

Materials synthesis. The Fe_2O_3 nanorods were synthesized by FeOOH nanorods template. To prepare FeOOH nanorods precursors, 1.9 mmol of $FeCl_3{\cdot}6H_2O$ was put into 15 ml of deionized water to form a homogeneous solution, then added 15 ml of 0.8 M NaOH solution under stirring, quickly. After stirring for 10 min, the total solution was transferred into a 50 ml Teflon-lined stainless steel autoclave, sealed and heated at 180 °C for 4 h. The result product was collected by centrifugation, washed with deionized water and ethanol, then was dried at 80 °C and calcined at 250 °C for 2 h. The Fe_2O_3 nanosheets were synthesized based on the previous work[28]. 5.1 mmol of $FeCl_3{\cdot}6H_2O$ was dissolved in 35 ml of anhydrous ethanol, and 38.4 mmol of $CH_3COONa{\cdot}3H_2O$ was rapidly added into the solution with stirring. After about 5 min of stirring, all of the reactants were transferred into a 50 ml Teflon-lined stainless steel autoclave, sealed and heated at 200 °C for 22 h. The result product was collected by centrifuge, washed with deionized water and ethanol. Then dried at 80 °C and calcined at 250 °C for 2 h.

Characterization. XRD measurements were performed on a Persee XD2 X-ray diffractometer with Cu-Kα radiation ($\lambda = 1.5418$). The size and morphology of all of the samples were measured with a S-4800 HITACHI scanning electron microscope (SEM) and a JEM-2100 transmission electron microscope (TEM). The specific surface areas of the powders were collected by a Gemini V Brunauer-Emmett-Teller (BET).

Electrochemical Measurement. For electrochemical studies, working electrode was fabricated with mixing active material, acetylene black and polyvinylidene fluoride (PVDF) with weight ratio 2:1:1 using N-methylpyrrolidone (NMP) as solvent. The slurry was fully ground and pasted onto copper foil, and then the loaded copper foil was dried in a vacuum oven at 120 °C for 12 h. Lithium metal, celgard 2300 membrane and 1 M $LiPF_6$ solution in DMC/EC (1: 1 in volume) were used as counter electrode, separator and electrolyte respectively to assemble coin cells in an Ar-filled glove box. The galvanostatic charge/discharge performance of the cells were tested on a battery testing system (BTS-5 V 5 mA, Neware) with the voltage between 0.1 and 3.0 V at the current density of 200, 400, 800, 1200, 1600, 2000, 2400 mA/g. The electrochemical spectroscopy (EIS) was tested with an (PGSTAT302N, Metrohm-Autolab) instrument using an amplitude of 5 mV and a frequency range from 100 KHz to 0.1 Hz. The PITT tests were also performed on the same instrument with EIS.

References

1. Poizot, P., Laruelle, S., Grugeon, S., Dupont, L. & Tarascon, J. M. Nano-sized transition-metaloxides as negative-electrode materials for lithium-ion batteries. *Nature* **407,** 496–499 (2000).
2. Ji, X., Lee, K. T. & Nazar, L. F. A highly ordered nanostructured carbon-sulphur cathode for lithium-sulphur batteries. *Nature Mater* **8,** 500–506 (2009).
3. Luo, J. *et al.* Rationally Designed Hierarchical TiO_2@Fe_2O_3 Hollow Nanostructures for Improved Lithium Ion Storage. *Adv Energy Mater* **3,** 737–743 (2013).
4. Ji, X., Herle, S., Rho, Y. & Nazar, L. F. Carbon/MoO_2 composite based on porous semi-graphitized nanorod assemblies from *in situ* reaction of tri-block polymers. *Chem Mater* **19,** 374–383 (2007).
5. Chen, W., Li, S., Chen, C. & Yan, L. Self-Assembly and Embedding of Nanoparticles by *in Situ* Reduced Graphene for Preparation of a 3D Graphene/Nanoparticle Aerogel. *Adv Mater* **23,** 5679 (2011).
6. Sun, X. *et al.* Three-Dimensionally " Curved" NiO Nanomembranes as Ultrahigh Rate Capability Anodes for Li- Ion Batteries with Long Cycle Lifetimes. *Adv Energy Mater* **4** (2014).

7. Ji, X., Evers, S., Lee, K. T. & Nazar, L. F. Agitation induced loading of sulfur into carbon CMK-3 nanotubes: efficient scavenging of noble metals from aqueous solution. *Chem Commun* **46,** 1658–1660 (2010).
8. Su, D., Dou, S. & Wang, G. Mesocrystal Co_3O_4 nanoplatelets as high capacity anode materials for Li-ion batteries. *Nano Res* **7,** 794–803 (2014).
9. Lee, H. S. *et al.* An organometallic approach for microporous organic network (MON)-Co_3O_4 composites: enhanced stability as anode materials for lithium ion batteries. *Chem Commun* **48,** 94–96 (2012).
10. Li, L., Guo, Z., Du, A. & Liu, H. Rapid microwave-assisted synthesis of Mn_3O_4-graphene nanocomposite and its lithium storage properties. *J Mater Chem* **22,** 3600–3605 (2012).
11. Ding, Y.-L., Wen, Y., van Aken, P. A., Maier, J. & Yu, Y. Rapid and Up-Scalable Fabrication of Free-Standing Metal Oxide Nanosheets for High-Performance Lithium Storage. *Small* **11,** 2011–2018 (2015).
12. Park, G. D., Lee, J.-H., Lee, J.-K. & Kang, Y. C. Effect of esterification reaction of citric acid and ethylene glycol on the formation of multi-shelled cobalt oxide powders with superior electrochemical properties. *Nano Res* **7,** 1738–1748 (2014).
13. Rui, K., Wen, Z., Lu, Y., Jin, J. & Shen, C. One-Step Solvothermal Synthesis of Nanostructured Manganese Fluoride as an Anode for Rechargeable Lithium-Ion Batteries and Insights into the Conversion Mechanism. *Adv Energy Mater* **5** (2015).
14. Qiu, H.-J., Liu, L., Mu, Y.-P., Zhang, H.-J. & Wang, Y. Designed synthesis of cobalt-oxide-based nanomaterials for superior electrochemical energy storage devices. *Nano Res* **8,** 321–339 (2015).
15. Li, G. *et al.* Controllable Synthesis of 3D $Ni(OH)_2$ and NiO Nanowalls on Various Substrates for High-Performance Nanosensors. *Small* **11,** 731–739 (2015).
16. Chen, J., Xu, L. N., Li, W. Y. & Gou, X. L. alpha-Fe_2O_3 nanotubes in gas sensor and lithium-ion battery applications. *Adv Mater* **17,** 582 (2005).
17. Sarradin, J., Guessous, A. & Ribes, M. Synthesis and characterization of lithium intercalation electrodes based on iron oxide thin films. *J Power Sources* **62,** 149–154 (1996).
18. Larcher, D. *et al.* Effect of particle size on lithium intercalation into alpha-Fe_2O_3. *J Electrochem Soc* **150,** A133–A139 (2003).
19. Cao, K. *et al.* 3D Hierarchical Porous alpha-Fe_2O_3 Nanosheets for High-Performance Lithium-Ion Batteries. *Adv Energy Mater* **5** (2015).
20. Morales, J., Sanchez, L., Martin, F., Berry, F. & Ren, X. L. Synthesis and characterization of nanometric iron and iron-titanium oxides by mechanical milling: Electrochemical properties as anodic materials in lithium cells. *J Electrochem Soc* **152,** A1748–A1754 (2005).
21. Larcher, D. *et al.* Combined XRD, EXAFS, and Mossbauer studies of the reduction by lithium of alpha-Fe2O3 with various particle sizes. *J Electrochem Soc* **150,** A1643–A1650 (2003).
22. Zhang, L., Wu, H. B. & Lou, X. W. Iron-Oxide- Based Advanced Anode Materials for LithiumIon Batteries. *Adv Energy Mater* **4** (2014).
23. Jain, G., Balasubramanian, M. & Xu, J. J. Structural studies of lithium intercalation in a nanocrystalline alpha-Fe2O3 compound. *Chem Mater* **18,** 423–434 (2006).
24. Wang, B., Chen, J. S., Wu, H. B., Wang, Z. Y. & Lou, X. W. Quasiemulsion-Templated Formation of alpha-Fe_2O_3 Hollow Spheres with Enhanced Lithium Storage Properties. *J Am Chem Soc* **133,** 17146–17148 (2011).
25. Wang, B., Wu, H. B., Zhang, L. & Lou, X. W. Self-Supported Construction of Uniform Fe_3O_4 Hollow Microspheres from Nanoplate Building Blocks. *Angew Chemi Int Edit* **52,** 4165–4168 (2013).
26. Islam, M. S., Driscoll, D. J., Fisher, C. A. J. & Slater, P. R. Atomic-scale investigation of defects, dopants, and lithium transport in the $LiFePO_4$ olivine-type battery material. *Chem Mater* **17,** 5085–5092 (2005).
27. Wei, G.-Z. *et al.* Crystal Habit-Tuned Nanoplate Material of $LiLi_{1/3-2x/3}Ni_xMn_{2/3-x/3}O_2$ for High-Rate Performance Lithium-Ion Batteries. *Adv Mater* **22,** 4364 (2010).
28. Yu, X.-Y. *et al.* Facet-dependent electrochemical properties of Co_3O_4 nanocrystals toward heavy metal ions. *Sci Rep* **3** (2013).
29. Xiao, X. *et al.* Facile Shape Control of Co_3O_4 and the Effect of the Crystal Plane on Electrochemical Performance. *Adv Mater* **24,** 5762–5766 (2012).
30. Lu, J. *et al.* Hematite nanodiscs exposing (001) facets: synthesis, formation mechanism and application for Li-ion batteries. *J. Mater Chem A* **1,** 5232–5237 (2013).
31. Grugeon, S., Laruelle, S., Dupont, L. & Tarascon, J. M. An update on the reactivity of nanoparticles Co-based compounds towards Li. *Solid State Sci* **5,** 895–904 (2003).
32. Chen, J. S. *et al.* Shape-Controlled Synthesis of Cobalt-based Nanocubes, Nanodiscs, and Nanoflowers and Their Comparative Lithium-Storage Properties. *Acs Appl Mater Inter* **2,** 3628–3635 (2010).
33. Xu, J.-S. & Zhu, Y.-J. Monodisperse Fe_3O_4 and gamma-Fe_2O_3 Magnetic Mesoporous Microspheres as Anode Materials for Lithium-Ion Batteries. *Acs Appl Mater Inter* **4,** 4752–4757 (2012).
34. Wang, Y., Takahashi, K., Shang, H. M. & Cao, G. Z. Synthesis and electrochemical properties of vanadium pentoxide nanotube arrays. *J Phys Chem B* **109,** 3085–3088 (2005).
35. Wu, C., Yin, P., Zhu, X., OuYang, C. & Xie, Y. Synthesis of hematite (alpha-Fe_2O_3) nanorods: Diameter-size and shape effects on their applications in magnetism, lithium ion battery, and gas sensors. *J Phys Chem B* **110,** 17806–17812 (2006).

Acknowledgements

This work was supported by the Beijing Nova Program (Z141103001814065), the Youth Innovation Promotion Association CAS (2016152), National Science Foundation for Young Scholars of China (21201177), the State Key Project of Fundamental Research (2014CB931900 and 2012CB932504).

Author Contributions

X.X. designed the experiments. M.C. and E.Z. performed the experiments, D.C. supervised the experiments, X.X., M.C. and E.Z. collected and analyzed the data, and wrote the paper. Z.H. gave suggestion to revise the manuscript. All authors analyzed data, discussed the results, and reviewed the manuscript.

Additional Information

Competing financial interests: The authors declare no competing financial interests.

How to cite this article: Chen, M. *et al.* The Effect of Crystal Face of Fe_2O_3 on the Electrochemical Performance for Lithium-ion Batteries. *Sci. Rep.* **6**, 29381; doi: 10.1038/srep29381 (2016).

This work is licensed under a Creative Commons Attribution 4.0 International License. The images or other third party material in this article are included in the article's Creative Commons license, unless indicated otherwise in the credit line; if the material is not included under the Creative Commons license, users will need to obtain permission from the license holder to reproduce the material. To view a copy of this license, visit http://creativecommons.org/licenses/by/4.0/